SEMON: Sensorless Event Monitoring in Self-Powered Wireless Nanosensor Networks

Eisa Zarepour[1] Mahbub Hassan[1] Chun Tung Chou[1]
Adesoji A. Adesina [2]

[1] School of Computer Science and Engineering
University of New South Wales, Australia
{ezarepour, mahbub, ctchou} @cse.unsw.edu.au

[2] ATODATECH LLC, Brentwood, CA 94513 USA
ceo@atodatech.com

Technical Report
UNSW-CSE-TR-201602
Feb 2016

THE UNIVERSITY OF
NEW SOUTH WALES

School of Computer Science and Engineering
The University of New South Wales
Sydney 2052, Australia

Abstract

A conventional wireless sensor network node consists of a number of components: microprocessor, memory, sensor and radio. Advances in nanotechnology has enabled the miniaturization of these components, thus enabling wireless nanoscale sensor networks (WNSN). Due to their small size, WNSN nodes are expected to be powered by harvesting energy from the environment. Unfortunately, there is a mismatch in the energy that can be harvested and the energy required to power all the aforementioned components in a WNSN node. In this paper, we propose a simplified sensor node architecture for event detection. We call our architecture SEMON which stands for Sensorless Event MONitoring in self-powered WNSNs. A SEMON node consists of only an energy harvester and a radio with minimal processing capacity. We assume that each event to be monitored will generate a different amount of energy and we can therefore use this amount of energy as the signature of an event. When an event occurs, a SEMON node harvests the energy released by the event and turns it into a radio pulse with an amplitude proportional to the harvested energy. A remote station is used to decode the amplitude of the pulse to recognize the event that has occurred. We propose two methods for the remote station to decode the events that have occurred. The first method is based on thresholds. The second method makes use of an event model which gives the probability that a sequence of events will occur. This enables us to formulate the decoding problem using Hidden Markov Models. We study the decoding performance of both methods. Finally, we provide a case study on using the SEMON architecture to monitor the chemical reactions inside a reactor.

1 Introduction

Nanosensors are emerging from the R&D cycle and we are about to witness their immediate use in existing macro devices, to reduce cost, power consumption, and weight while achieving high sensitivity. In this paper we will refer to this imminent trend as *nano-for-macro*, as the nanotechnology is basically used to improve the quality of the macro sensor networks. Table 1.1 compares the power consumption of some nanosensors against their macro counterparts. As we can see, nanosensors consume between nW-μW, considerably less than conventional macrosensors.

Nevertheless, realizing *nano-for-nano* — such as wireless nanoscale sensor networks (WNSN) [3] — where nanosensors will be housed in small microscopic devices to produce functional nanomotes, faces challenges. A major issue facing the realization of *nano-for-nano* is how to power onboard nanosensors, given the extraordinary space limitations of a nanomote to house power supply. Although the power consumption of nanosensors is considered "ultra-low" for nano-for-macro, it is considered prohibitively high relative to what can be practically supplied on a tiny nanomote. For example, the most recently developed nanomaterial-based energy harvesting circuits have power density ranges between 1mW [49] and 4.5W [57] per cm^{-3}, which may be adequate to generate enough power in a macro device for an onboard nanosensor, but would generate only one femto to a few pico W in a microscopic device, due to the severe volume restrictions. This means that we do not have a powering solution for nanosensor networks that can be adequately duty cycled to meet the high-resolution monitoring requirements of nano-for-nano applications.

In this paper, we propose SEMON, which stands for Sensorless Event MONitoring, to overcome this problem. SEMON attempts to monitor events in the environment without employing any onboard sensors, which technically solves the sensor powering problem in a nanomote. It is based on the following idea. We observe that there are many biological and chemical events of interest that dissipate energy in some forms when they take place. The amount of energy released varies depending on the type of event, creating an opportunity to detect and monitor those events from their emitted energies. Given that we now have a variety of nanoscale energy harvesters capable of harvesting many different types of energy, it should be possible to harvest that energy not only to use it as a source of powering the nanomote, but also to detect the events at the same time. Using the instantaneous harvested energy to transmit a short pulse of proportional amplitude, SEMON enables sensorless event detection and monitoring at a remote macro station.

Because the harvestable power at a nanomote is very small and the terahertz waves — the operating frequency of nanoscale antennas [21] — are subject to severe attenuation and noise due to molecular absorption, a key performance issue of SEMON is the maximum distance (called 'monitoring distance' in this paper) at which events can be monitored with high reliability. We study the monitoring distance as a function of many physical parameters, such as the number of distinct event types and the amount of harvested energy. We find that for the range of harvestable power at nanoscale, SEMON enables reliable event detection at distances from a few centimeters up to a meter depending on the number of events to detect. Our contributions in this paper are summarized as follows:

- We propose a novel sensorless event-monitoring architecture for wireless nanosensor networks, which addresses the sensor powering issue in a nanomote, enabling immediate realization of nano-for-nano applications.
- We demonstrate that simple threshold-based symbol detection (TBD) can be deployed at the remote station to monitor completely unknown environments with no *prior* knowledge of the event model.
- We propose a Hidden Markov Model (HMM)-based decoder at the remote station that can outperform the TBD. We demonstrate that if *a priori* knowledge of event transition probabilities is available, HMM-based detection can significantly reduce the event detection error and extend the monitoring distance by several orders of magnitude compared to the TBD-based decoder.
- Finally, we propose and validate a novel application of SEMON for high-resolution monitoring of chemical reactors at the molecular level.

Table 1.1: Power consumption of different types of sensors in both nano-scale and macro-scale

Category	**Nano sensors**		**MEMs or macro sensors**	
	Type	**Power consumption**	**Type**	**Power consumption**
Gas Sensors	Hydrogen sensor	1 nW [10] 0.1 uW [35], 15 uW [44]	Hydrogen sensor	660 mW [11]
	NO2 sensor	10 uW [38]	NO2 sensor	20 mW [43]
	Methane sensor	4 nW - 4 uW [5]	Ethanol sensor	286mW [32]
Biomedical sensor	Glucose biosensor	0.1 uW [25]	Glucose	3 uW [29] 11 mW [26]
Pressure &	Pressure sensor	1 nW [20] - 1 uW [55]	Zigbee sensor node	2.5 mW [41]
Temperature Sensors	Temperature sensor	1 nW [30]	Zigbee sensor node	0.3 mW [40]

The rest of the paper is structured as follows. The literature on designing sensor-less mechanisms and HMM-based decoders is reviewed in Section 2. Section 3 provides a critical examination of the sensor powering bottleneck in nanomotes. SEMON is presented and motivated in Section 4, followed by its performance evaluation in Section 5. A novel application of SEMON in industrial chemistry is presented and analyzed in Section 6. The paper is concluded in Section 7.

2 Related work

Sensorless sensing has been demonstrated in the literature at both macro and nanoscale. At macroscale, a few sensorless monitoring approaches have been proposed, mainly for condition monitoring of instruments. In one category of research, the amount of power consumed by a machine was used as a signature

to monitor the machine's status without using any sensors [13, 28]. For example, Alfonso et al. used the current of the spindle motor of a drilling machine as a source to recognize defects in the machine [13]. In another category of the research, a sensorless internal temperature monitoring method for induction motors was proposed [42, 56]. As stator winding resistance varies with variation in the temperature, it can be used as a signature to monitor internal temperature of the induction motors [42]. Finally, Khalifa et al. have recently demonstrated that human activity can be recognized by analyzing the AC voltage generated by a piezoelectric vibration energy harvester housed in a wearable device [22, 23]. Unlike our proposed framework, these studies provide no solution to *remotely* monitor the condition.

In addition, at the nanoscale, two works study the use of the energy harvesting interface as a sensor at nanoscale [51, 54]. Yang and others have shown that a pyroelectric nanogenerator made from a single nanowire of zirconate titanate can play a role as a temperature sensor. The output voltage of the nanogenerator linearly increases with an increasing rate of change in temperature, so it can be used to infer the temperature [51]. In [54], a triboelectric nanogenerator (TENG), based on the well-known contact electrification effect, has been used as a gas sensor. As the amount of power that can be harvested via a TENG is strongly affected by its surface adsorbed molecules, different types of molecules can be efficiently detected merely by monitoring the output voltage of the TENG [54]. In these two works, similar to our approach, the energy harvester is used as a sensor. However, the sensed data (detected temperature or gaseous species) will not be transferred to a remote station, which is the main objective of sensor networks. Remote sensorless event monitoring over terahertz channel were first discussed in our preliminary work [53] in the context of nanoscale monitoring of chemical reactors. In this work, we present and analyze a more generalized architecture of such systems and propose a HMM-based decoder that provides accurate event detection at longer distances.

As we use HMMs to increase the accuracy of event detection, we highlight few related works in this area. Using HMM to estimate the quality of a wireless channel and for signal classification is well-established [39]. For example, in [24] a binary HMM was trained via Baum-Welch Algorithm (BWA) to detect received signals based on real signal traces. The BWA provides an efficient method for calculating the parameters of a HMM given an observed (or simulated) data set of events. In this work, the states are the peaks of the signal and the observations are the detected energy levels at the receiver. By using a sequence of 300 observation, the accuracy of the signal detection via a given modulation schema (BPSK) can be improved from 50% to 100% for a given signal-to-noise ratio (SNR) of -3dB. Although our approach to using a HMM to increase the accuracy of event detection is conceptually similar to this work, it has two main differences. First, the channel in these studies is assumed to be a Rayleigh fading channel, which is different from our terahertz channel model. Second, our *observations* are not discrete and have continuous Gaussian distributions.

In wireless sensor networks, HMMs were also employed to increase the accuracy of human activity recognition via body area sensor networks [47, 27, 14]. For example, Wei et al. proposed a HMM for a wearable body sensor network whose states are 8 human activities and its emissions are the accelerometer outputs for those activities [47]. They used BWA to train the system and Viterbi

Table 2.1: Few existing solutions for harvesting energy at the nano-scale.

Energy source	**Technology**	**Power Density ($\mathbf{pW/\mu m^3}$)**	**Structure**
Mechanical energies	Piezoelectric	0.5	ZnO_2 nano wires [46]
		1.1	Verticaly align ZnO_2 nano wires (length 5nm, diameter:200nm) [58]
		0.8	A 550nm thick $BaTiO_3$ thin film [37]
		2.8	PZT nanowire array (Length $5mum$ and diameter of $500nm$) [48]
	Triboelectric	2.1	[18]
	Piezoelectric and triboelectric	1.1	Using PVDF, nanostructured Al and MNDS [18]
	Instantaneous discharging triboelectric	3.6	SiO_2 NPs assembled on a Au film [8]
Thermal	Pyroelectric	0.05	Using ZnO_2 nanowires of 1 μ length [49]
		0.1	Using liquid-based switchable thermal interfaces [7]
		3	Using BaTiO3 film of 200nm thick [6]
Magnetic force	Magnetic-assisted triboelectric	0.5	Is achieved by coupling between the triboelectric effect and the electrostatic induction [19]
Magnetic force and vibration energy	Magnetoelectric	4.5	A piezoelectric fibre composite bonded to a Ni cantilever [57]

algorithm [12] to decode the most probable series of activity, with an accuracy of 95.82%. Our approach differs from these methods in a few different aspects. Firstly, the article [47] uses the HMM in the sensor node to reduce the transmission rate between the sink and the sensor node, which is not applicable to WNSN due to computational limitations. Secondly, the observations are deterministic (the accelerometer output), but in our architecture the received signals at the sink (observations) would be probabilistic due to Gaussian distribution of noise in the channel. In most of these studies, the sensor node has all conventional components such as microprocessor, memory, etc., and is not necessary self-powered, while our design is more appropriate for energy harvesting sensor networks. Finally, they do not consider the restriction of WNSN, so their contributions might not be directly applicable to WNSN.

3 Sensor powering bottleneck in nanomotes

For wireless sensor networks, there are two fundamental solutions for power supply; battery and energy harvesting. Battery is less practical at nanoscale because it is not possible to house a large battery in a nanomote for prolonged operations of the network and it is impractical to replace batteries at microscopic level. Energy harvesting is therefore the most practical option. Although we have seen in Table 1.1 that the power consumption of nanosensors is significantly lower than that of macrosensors, to put things into perspective we must compare these consumption figures with what can be harvested in nano-for-nano, given the extraordinary space limitations of a nanomote.

Table 2.1 shows the amount of power that can be harvested using different combinations of energy source and transduction technique for a 1 cubic micron volume, which would be a reasonable percentage of the total volume of a nanomote via an average excitement applied to the harvester. A quick comparison between Tables 1.1 and 2.1 reveals that for most sensors the power consumptions of nanosensors are many orders of magnitude higher than what could possibly be harvested. The problem is exacerbated by the fact that in many applications an array of sensors may be required to accurately detect a complex event, which would consume even more power. The only way to operate would then be to duty cycle the nanomotes at an extremely low rate, i.e., leave them in sleep or inactive mode for most of the time. Given that many nanoscale events of practical interest usually occur at a very high frequency, such low duty cycling would defeat the purpose of developing microscopic sensor networks in the first place.

It is clear that the high consumption-to-harvesting power ratio of a nanomote severely limits the applicability of nanoscale sensor networks. Novel sensing mechanisms are needed for nanomotes to realize their full potential. In the following section, we propose a sensorless monitoring architecture for nanomotes that achieves event detection in an energy-harvesting sensor network without the help of any sensors.

4 The SEMON Architecture

In the conventional self-powered wireless sensor network (WSN) architecture, energy harvesting is used to recharge a battery or accumulate energy in a capacitor to simultaneously power all elements of a WSN node, which includes a microprocessor for processing data and communication algorithms, a memory for temporary storage of data, one or more sensors to measure the relevant physical variables of the environment, and a radio for transmitting measured data to the sink. In contrast, a SEMON node has only two components: an energy harvester and a radio with some minimal in-built processing capability. This section explains how this simplified node architecture enables event detection.

4.1 Working Principle

Let us consider an environment monitoring task which requires the deployment of nanomotes at specific locations to monitor the occurrence of a known set of events. Each nanomote is to collect the relevant data and send them wirelessly

to a remote station that processes the data to infer the type and timing of the events that have occurred. We assume that each event emits a certain amount of energy when it occurs, which can be harvested using a suitable nanoscale energy harvester onboard the nanomote. We further assume that the amount of energy generated by an event depends on the type of event. If different events generate different amounts of energy, then conceptually, it is possible to use the harvested energy as a signature for event recognition. The SEMON architecture is based on this concept.

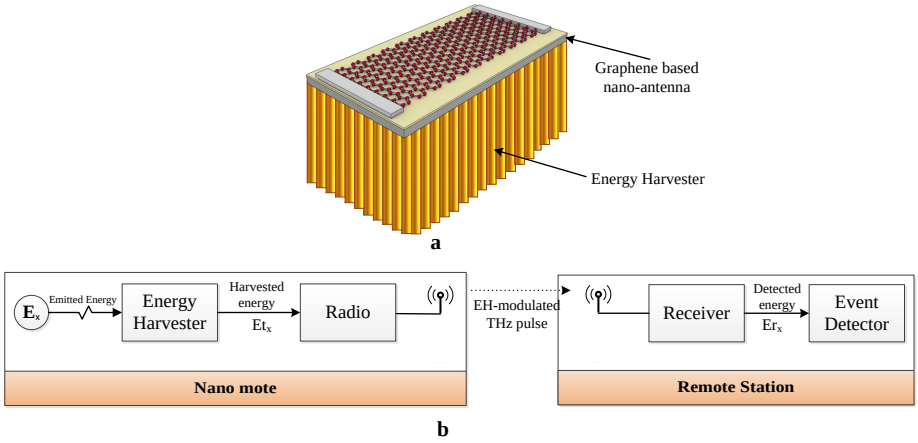

Figure 4.1: (a) Conceptual drawing of a SEMON nanomote. (b) Schematic of the SEMON architecture which includes a nanomote and a remote station.

Figure 4.1 shows the schematic of the SEMON architecture, which consists of a nanomote and a remote station. The nanomote, which consists of an energy harvester and a nanoradio[1], is located at where the events take place. If an event occurs, the energy emitted by the event is first harvested and then used in its entirety to power a radio pulse transmission in the terahertz band using the onboard nanoradio. The pulse amplitude is, therefore, implicitly modulated by the amount of energy harvested or emitted by the event. At the remote station (receiver or sink) the pulse energy is detected by integrating the received energy over an interval using widely used pulse energy detection methods [17]. Because different events emit different amounts of energy, the remote station detects the events from the detected energy at the receiver.

4.2 Event Detection

Event detection at the receiver is non-trivial. Due to the molecular absorption and random noise of the terahertz band, the detected energy of a given transmitted pulse becomes a random Gaussian variable. The detected energy of different events then overlap with each other, making accurate event detection a challenging problem. We propose and compare two different event detection algorithms for SEMON. The first algorithm assumes no *prior* knowledge of the event model

[1]We may need some built-in processor in the radio module to drive the antenna, i.e., generate the Gaussian pulse.

and employs a simple energy threshold-based algorithm. The second algorithm assumes *a priori* knowledge of event transition probabilities and uses a HMM to reduce event detection errors. Before describing these two algorithms, we first present the event model and the receiver model.

Event model

Our aim is to use SEMON to monitor a set of M possible event types $s_1, s_2, \ldots, s_M$. We assume that when an event of type s_i occurs, it emits $E_{e,i}$ amount of energy and all $E_{e,i}$'s are distinct. For a reason which will become clear in Section 4.3, we assume that the event types are ordered in ascending order of event emission energy, i.e. $E_{e,1} < E_{e,2} < ... < E_{e,M}$.

Let q_t denote the t-th event that has occurred where $t = 0, 1, 2, ...$ This means that the sequence of events that has occurred is $[q_0, q_1, q_2, ...]$ where each q_t is one of $s_1, s_2, \ldots, s_M$. (Note that t is used to index the events and the inter-event time is not necessarily a constant.) We assume that the sequence of events is a realization of a Markov chain. This is a fairly natural model. For example, the evolution of a set of chemical reactions can be modeled by a continuous-time Markov chain (CTMC) [16] where state transitions are caused by chemical reactions; these chemical reactions are the events and we can model the sequence of events by using an embedded Markov chain formed by the state transitions of CTMC.

Our event model is therefore a Markov chain specified by an initial probability distribution of π and the transition probability matrix of T. We use $\pi_i = P(q_0 = s_i)$ to denote the probability that the first event is from type s_i. The transition probability $t_{i,j}$ is

$$t_{i,j} = P(q_t = s_j | q_{t-1} = s_i) \text{ for } t \geq 1$$

Receiver model

The receiver model aims to characterize the signal received by the remote station. When an event of type s_i occurs at the nanomote, it generates an amount of energy equals to $E_{e,i}$. We assume both the energy harvester and the nanoradio are ideal, which means the nanomote generates a pulse with energy $E_{e,i}$ to be transmitted to the remote station. (Note that inefficiency in energy harvesting and radio can be taken care of easily.) We further assume that the pulse generated by the nanoradio has a duration of $T_p = 10^{-13}s$ and its power spectral density (PSD) uniformly spread in the 0.1-10 THz band. We denote $B = 10$ THz as the bandwidth of the pulse and $U_i(f)$ as the PSD of the transmitted signal at frequency f when event type s_i occurs.

A key problem in using the terahertz band for communication is that molecular absorption creates a noisy communication channel. We assume the transmission medium has X types of molecules which are indexed by x, molecule type x has a mole fraction of m_x and absorption coefficient at frequency f is $K_x(f)$. The molecular absorption coefficient $K(f)$ of the medium at frequency f is the weighted sum:

$$K(f) = \sum_{x=1}^{X} m_x K_x(f) \tag{4.1}$$

Note that the absorption coefficients $K_x(f)$ of individual molecule species can be obtained from the HITRAN database [4].

Let d denote the distance between the nanomote and the remote station. The total attenuation due to spreading and molecular absorption at frequency f at a distance d from the radio source, $A(f,d)$, is given by [21]:

$$A(f,d) = \left(\frac{4\pi f_0 d}{c}\right)^2 e^{K(f)d} \tag{4.2}$$

where $f_0 = \frac{B}{2}$ is the centre frequency and c is the speed of light.

The PSD of the received signal $P_{r,i}(f,d)$ at frequency f and distance d is:

$$P_{r,i}(f,d) = \frac{U_i(f)}{A(f,d)} \tag{4.3}$$

The average received energy for a given event of s_i then would be:

$$E_{r,i}(d) = \int_B P_{r,i}(f,d) T_p df \tag{4.4}$$

where T_p is the duration of the transmitted pulse in second. The PSD of the molecular absorption noise $N_{\text{abs}}(f,d)$ which is due to the re-radiation of absorbed radiation by the molecules in the channel is given by [21]:

$$N_{\text{abs}}(f,d) = k_B T_0 (1 - \exp(-K(f) * d)) \tag{4.5}$$

where T_0 is the reference temperature 296K and k_B is the Boltzmann constant. Assuming a flat noise spectrum, the noise PSD at distance d would be:

$$N(d) = \frac{\int_B N_{\text{abs}}(f,d) df}{B} \tag{4.6}$$

The remote station uses an energy detector (ED) to determine the energy level of the received signal. The ED requires the design of a filter, matched to the received pulse shape. We assume the bandwidth of the filter is equal to B. If an event of type s_i occurs at the nanomote, the received energy level has a Gaussian distribution of g_i with mean μ_i and variance σ_i^2 given by [9]:

$$\mu_i = N T_{\text{int}} B + E_{r,i} \tag{4.7}$$

$$\sigma_i^2 = N^2 T_{\text{int}} B + 2N \times E_{r,i} \tag{4.8}$$

where N is the noise PSD at distance d that can be calculated from Eq. (4.6), $E_{r,i}$ is the average received energy for symbol s_i that can be calculated from Eq. (4.4). T_{int} is the integration time which is a design parameter, typically $T_{\text{int}} \geq T_p$.

4.3 Threshold-based event detection

This section presents the threshold-based decoder (TBD) which uses the received energy at the remote station to determine the event that has occurred at the nanomote. TBD uses only the current received energy and does not use the history of past received energy. Recall from Section 4.2 that if event type s_i has

occurred, then the received energy has a Gaussian distribution with mean μ_i and variance σ_i^2 given in Eq. (4.7) and (4.8). Also, recall from Section 4.2 that for two event types s_i and s_j with $i < j$, we have $E_{e,i} < E_{e,j}$ where $E_{e,i}$ and $E_{e,j}$ are respectively the energy emitted when the event types s_i and s_j occurs. Consequently, we have $\mu_i < \mu_j$ for $i < j$ or the mean received energies μ_i are sorted in ascending order.

In order to distinguish between the M event types, we need $M-1$ different thresholds, which are denoted by $\xi_{1,2}$, $\xi_{2,3}$, ..., and $\xi_{M-1,M}$. The value of $\xi_{i,j}$ ($i = 1, ..., M-1$ and $j = i+1$) is given by the intersection of the Gaussian density functions with parameters (μ_i, σ_i^2) and (μ_j, σ_j^2), i.e. $\xi_{i,j}$ satisfies

$$\frac{1}{\sqrt{2\pi}\sigma_i} e^{\frac{-(\xi_{i,j}-\mu_i)^2}{(2\sigma_i^2)}} = \frac{1}{\sqrt{2\pi}\sigma_j} e^{\frac{-(\mu_j-\xi_{i,j})^2}{(2\sigma_j^2)}} \tag{4.9}$$

and we have $\mu_i < \xi_{i,j} < \mu_j$.

Let e_r be the received energy at the remote station, then the estimated event type $\hat{i}$ is determined according to:

$$\hat{i} = \begin{cases} 1 & \text{if } e_r < \xi_{1,2} \\ i & \text{if } \exists i \in \{2, 3, ..., M-1\} \ s.t. \ \xi_{i-1,i} < e_r < \xi_{i,i+1} \\ M & \text{if } e_r > \xi_{M-1,M} \end{cases} \tag{4.10}$$

It can be shown that the error probability $P_{e,TBD}$ of the TBD method is given by:

$$P_{e,TBD} = P[E_r > \xi_{1,2}|s_1]P[s_1] \tag{4.11}$$

$$+ \sum_{i=2}^{M-1} (P[E_r < \xi_{i-1,1}|s_i] + P[E_r > \xi_{i,i+1}|s_i])P[s_i]$$

$$+ P[E_r < \xi_{M-1,M}|s_M]P[s_M] \tag{4.12}$$

where $P[s_i]$ is the probability that event type s_i occurs, E_r is the random variable of received energy at the remote station and $P[E_r > \xi|s_i]$ is the conditional probability that the received energy is greater than ξ given that the event type s_i has occurred. Note that the conditional probability is in fact a Gaussian distribution with mean μ_i and variance σ_i^2. Therefore, given the event model and the receiver model, it is possible to determine the classification error.

4.4 HMM-based event detection

The TBD method does not use the past history of received energy for event detection and classification. The classification accuracy of TBD can be improved by using the past history of received energy as well as the event model at the remote station. Given that the evolution of events can be modeled by a Markov chain and the received energy can be modeled by a Gaussian distribution for any event type, the classification problem can be modeled by a HMM. In particular, the sequence of events $q_0, q_1, q_2, ...$ occurring at the nanomote is the unknown state of the HMM and the evolution of q_t is governed by the event model. Each unknown event q_t generates a pulse which is received by the remote station. Let $e_{r,t}$ be the energy received by the remote station when the t-th event has occurred. We consider an event window of size W consisting of the sequence

of received energies $[e_{r,t}, e_{r,t+1}, ..., e_{r,t+W-1}]$. Our aim is to use HMM to determine the most likely event sequence $[q_t, q_{t+1}, ..., q_{t+W-1}]$ that gives rise to the sequence of received energies. This problem can be solved by the Viterbi algorithm [12].

5 Performance evaluation of SEMON

This section aims to study the accuracy of event detection using SEMON. We first explain the methodology, then followed by the event detection results for TBD and HMM-based decoders.

5.1 Methodology

We assume that a SEMON node is used to monitor M distinct events. These events occur in random order and are generated by an embedded Markov chain with initial probability distribution π and transition probability matrix T, as described in the event model in Section 4.2. We further assume that the initial probability of each event is the same, i.e. $\frac{1}{M}$ because there are M events. This probabilistic event model allows us to generate many possible event sequences. After generating an event sequence, we use the receiver model in Section 4.2, in particular Eq. (4.7) and (4.8), to derive the probability distribution of the received energy at the remote station of each event.

We investigate the performance of two decoders: TBD and HMM. For TBD, the classification rule is given by Eq. (4.10) and the error probability is computed by Eq. (4.12). For HMM, we use the HMM Toolbox for Matlab [36] which implements the Viterbi algorithm. We input both the event model and measurement model (i.e. Gaussian distribution of the received energy) to the Viterbi algorithm to determine the most probable path through the HMM states. In order to vary the SNR, we will vary the average harvestable power of the M events, which is denoted by E_H. The distance d between the nanomote and the remote station will also be varied. Unless otherwise stated, we assume these default parameters: $M = 4$, standard air composition for the transmission medium and $E_H = 1$pW.

5.2 Performance of threshold-based detector

In this Section, we assume the power levels generated by the events are 0.25, 0.75, 1.25 and 2 pW. With these power levels and the receiver model, we plot in Figure 5.1 the Gaussian distributions of the received power for two values of d: 2mm and 4mm. The figure shows that for a higher distance d, the average received energy is lower for each event type and there is more overlap of the Gaussian distributions. This is due to higher attenuation and higher noise for a larger d. The probabilities of incorrect classification for 2mm and 4mm are, respectively, 9% and 37.9%.

We now study how the distance d impacts on the classification error. Figure 5.2 plots the classification error against distance d. The error remains small for $d \leq$ 2mm but beyond that, the error increases rapidly and becomes very high for large distance d. The shape of the curve can be understood by the fact

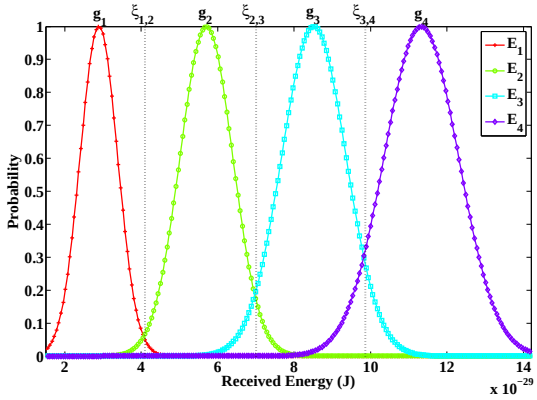

(a) $d = 2mm$, $P_{e,TBD} = 0.09$, Noise=1.5aW, Pathloss=52dB

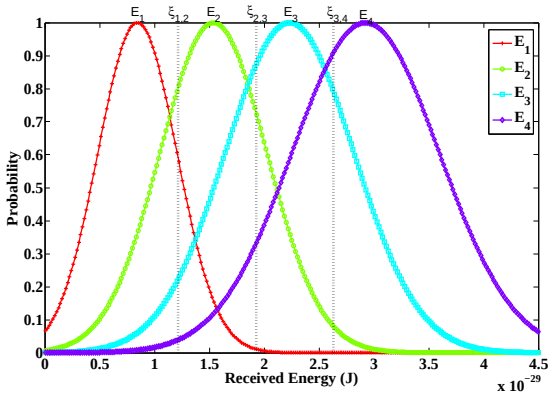

(b) $d = 4mm$, $P_{e,TBD} = 0.38$, Noise=3aW, Pathloss=58dB

Figure 5.1: The received energy distribution for $M = 4$ event types. (a) $d =$ 2mm. (b) $d = 2$mm.

that noise and attenuation in a terahertz channel increases exponentially with distance, as shown in Eq. (4.5) and (4.2).

The distance at which events can be decoded accurately is an important factor in any remote environmental monitoring task. Thus we define the *monitoring distance*, η, as the maximum distance at which all events can be detected with less than 10% error. We now study the impact of different parameters on the achievable monitoring distance using TBD. The parameters that we consider are: (1) Mean absorption coefficient of the transmission medium; (2) The number of events; and, (3) The average harvestable power E_H. In this study, we vary one of these three parameters at a time. The parameters that we do not vary will take on the default value: the mean absorption coefficient is that of standard air, $M = 4$, and $E_H = 1pW$. Figure 5.3a shows the effect of mean absorption coefficient of the transmission medium on the monitoring distance η. We vary the absorption coefficient by changing the chemical composition

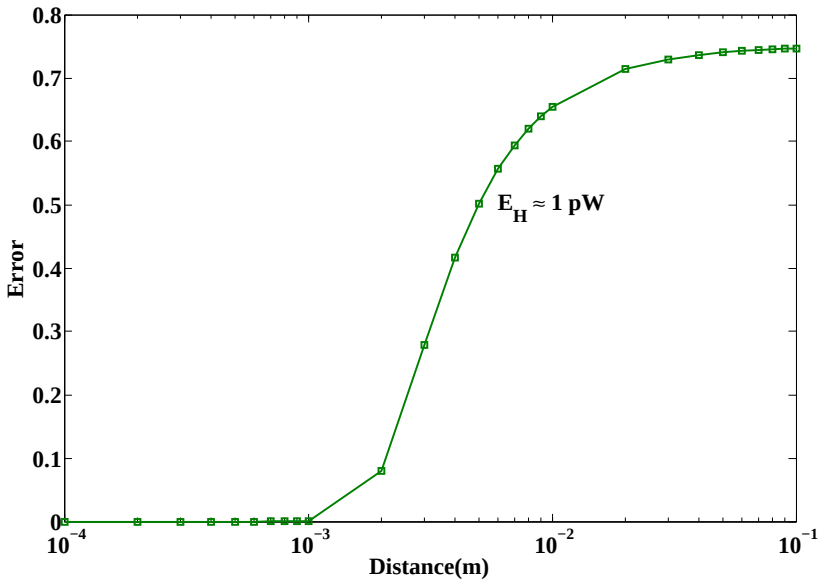

Figure 5.2: The effect of distance on the accuracy of event detection with $E_H \approx 1pW$.

of the transmission medium. On a log-log plot, the monitoring distance η decreases linearly with increasing absorption coefficient. We next vary the number of events from 2 to 1000. Figure 5.3b shows that the monitoring distance is a decreasing function of the number of events M. Lastly, Figure 5.3c shows the monitoring distance as a function of average harvestable power varies between 1fW and 1nW. This figure highlights the limitation of the TBD as the maximum η is limited to 2cm even if SEMON can harvest around 100pW on average; we will show later on that the HMM decoder can improve the performance.

5.3 Performance of HMM-based decoders

The main difference between the TBD and HMM decoders is that the HMM decoder makes use of the event model for decoding. As a start, we want to understand when an event model will be useful. On one extreme, if the events take place in a predictable order, then the event model will be useful. On the other extreme, if the events occur randomly, then the event model will not be of much use; and, we expect TBD and HMM decoders to have similar performance because the HMM decoder cannot exploit the event model. We would like to quantify this intuition. Recall that the event model is assumed to be a Markov chain with initial state probability π and transition matrix $T = [t_{i,j}]$. Let ζ_i denote the stationary probability of being in state i. We can quantify the uncertainly of a Markov chain by its entropy Φ, which is given by

$$\Phi = -\sum_{i=1}^{M} \zeta_i \times \sum_{j=1}^{M} t_{i,j} \times \log_2(t_{i,j}) \tag{5.1}$$

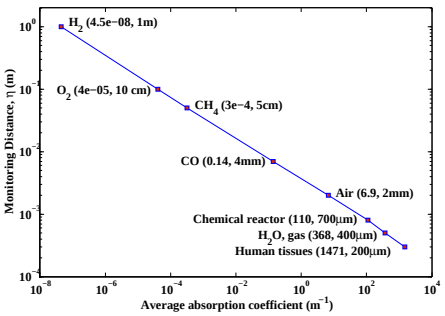

(a) The monitoring distance in different channel compoistions (M=4, $E_H = 1pW$).

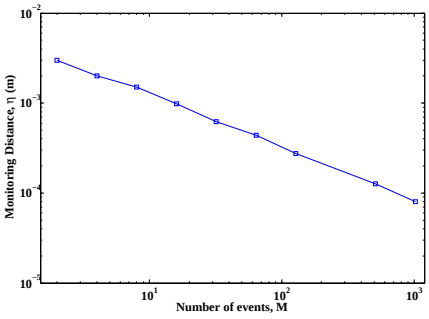

(b) The effect of the number of events on the monitoring distance (Standard air in the medium and $E_H = 1pW$).

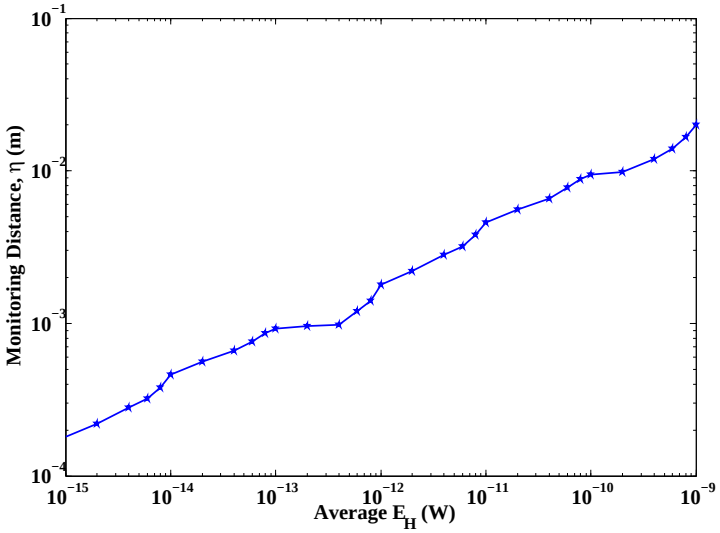

(c) The effect average harvestable power via different events on the monitoring distance (Standard air in the medium and M=4).

Figure 5.3: Monitoring distance, η (error<10%) as a function of different parameters.

For a Markov model with M states, its entropy varies between 0 and $log_2 M$ where an entropy of $log_2 M$ means the events appear randomly or $t_{i,j} = \frac{1}{M}\ \forall i, j$. In order to investigate the effect of the entropy Φ on the performance of the HMM decoders, we assume $M = 4$ and consider ten scenarios with ten different entropies ranging from 0 to 2:

$$T_1^{\Phi=0} : \begin{pmatrix} 0 & 0 & 0 & 1 \\ 0 & 0 & 1 & 0 \\ 1 & 0 & 0 & 0 \\ 0 & 1 & 0 & 0 \end{pmatrix}, T_2^{\Phi=0.15} : \begin{pmatrix} 0.01 & 0.01 & 0.01 & 0.97 \\ 0.01 & 0.01 & 0.97 & 0.01 \\ 0.97 & 0.01 & 0.01 & 0.01 \\ 0.01 & 0.97 & 0.01 & 0.01 \end{pmatrix}, \ldots, T_{10}^{\Phi=2} : \begin{pmatrix} 0.25 & 0.25 & 0.25 & 0.25 \\ 0.25 & 0.25 & 0.25 & 0.25 \\ 0.25 & 0.25 & 0.25 & 0.25 \\ 0.25 & 0.25 & 0.25 & 0.25 \end{pmatrix}$$

For each scenario, we assume the mean harvestable power is 1pW and distance between the nanomote and remote station is $50cm$. For each scenario, we use

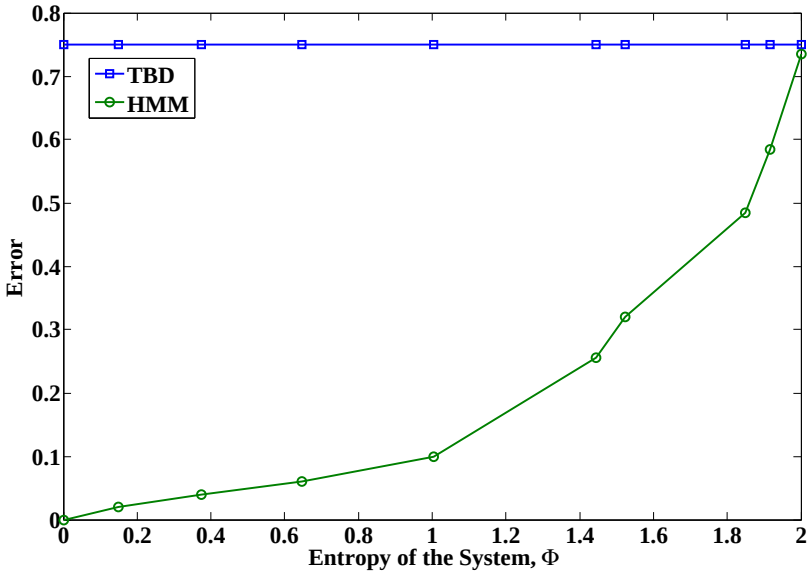

Figure 5.4: The effect of the entropy of the events on the performance of the HMM-based decoder (M=4, distance=50cm, E_H=1pW and medium is standard air).

the event model to generate 50 sequences of 100 events, and then generate the observations using the receiver model. For decoding, we use both HMM and TBD. For HMM, we assume the entire sequence of observations is available. Figure 5.4 plots the event detection error against entropy. The figure shows that the error rate of the HMM decoder increases with the entropy. If the order of events are fairly predictable (low entropy), then the error rate is low. If the order of events are very random (high entropy), then HMM and TBD decoders give similar error rates. The figure also shows that HMM-decoder performs better than TBD-decoder for all values of entropy.

In the earlier study, we assume that the HMM decoder uses the entire sequence of observations for decoding. In this study, we introduce a window size parameter W. With a window size W, the HMM decoder waits for W observations to arrive and then proceed to decode the sequence of W observations. The decoder will then wait for another W observations before starting the decoding process again. A large W means the HMM-based decoder will have more opportunity to use the underlying probabilistic model to improve the detection process. To study the effect of window size on the performance of the HMM decoder, we generate 50 sequences with 200 events each; the other parameters being: $M = 4$, $E_H = 1$pW, $d = 50$cm, event model entropy $\Phi = 1$. We vary the window size W from 1 to 200. Figure 5.5 shows the average error over 50 realizations of event sequence. For a small W, the HMM and TBD decoders have similar performance; this is due to a lack of opportunity to use the event model. The error rate decreases with increasing W, but the error rate reaches a plateau beyond a certain value of W. It appears that there is not much benefit

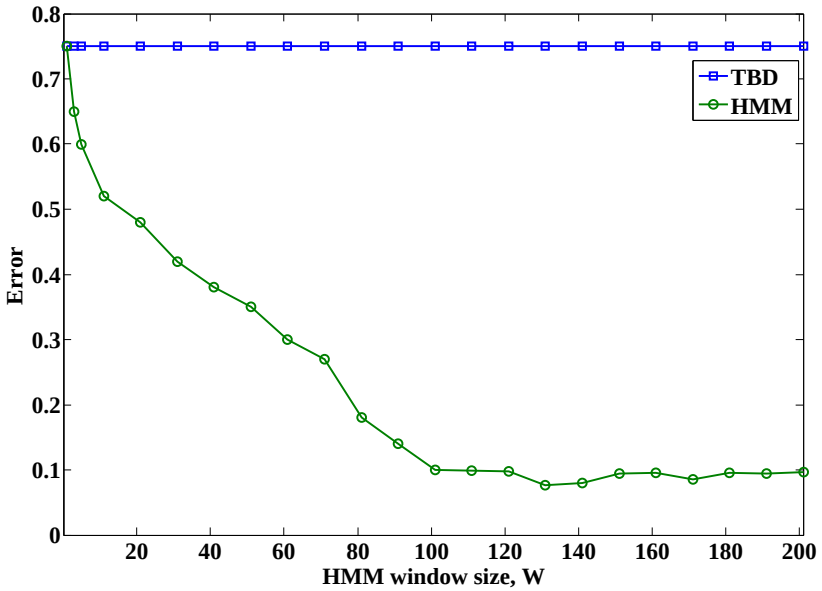

Figure 5.5: The impact of selecting appropriate window size on the performance of the HMM based decoders. The higher window size, the lower error (M=4, distance=50cm, E_H =1pW, $\Phi = 1$) and standard air in the wireless channel.

to increase the window size beyond a certain value.

Finally, we investigate the maximum monitoring distance η that can be achieved via both TBD and HMM-based decoders with these parameters: standard air as the medium, M=4, $\Phi \approx 1$ and E_H=1pW. Figure 5.6 shows that HMM can significantly improve the η by around three orders of magnitude. It shows a monitoring distance up to 50 cm can be achieved using a harvestable power at 1 pW.

Our earlier investigation shows that it is advantageous to use the HMM decoder when the events to be monitored are not completely random. In fact, natural events inherently are not completely random and the correlation between events is considerable. In the next section we study a real environmental monitoring task in which a SEMON nanomote is used to monitor chemical reactions within a chemical reactor at the molecular level.

6 An application of SEMON in industrial chemistry

Because of the extremely small form factor of nanosensors, researchers are considering deploying them in embedded environments to observe physical phenomena at the molecular scale. Monitoring chemical processes within a reactor for the possibility of controlling the process from the bottom up is one such application recently discussed in industrial chemistry literature [52]. However, the work in [52] assumed that the nanosensor nodes have continuous power sup-

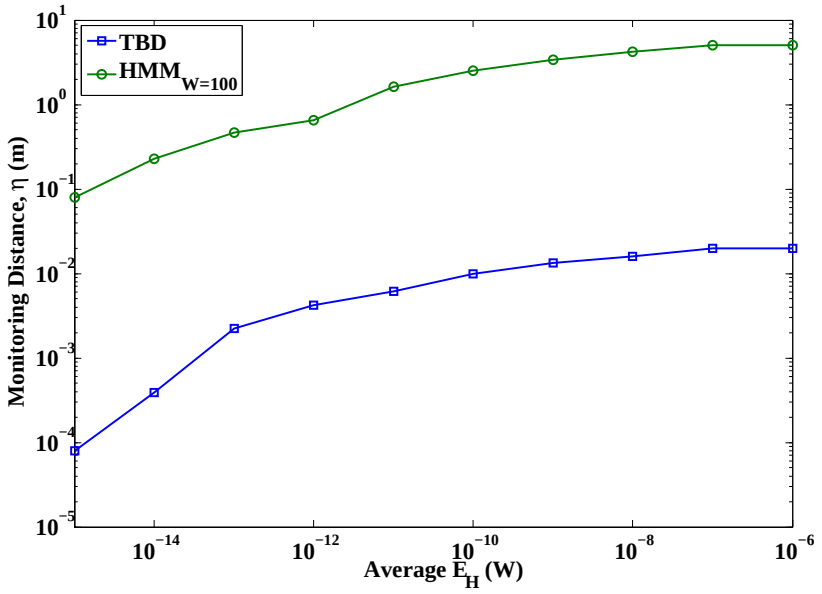

Figure 5.6: The monitoring distance as a function of average harvestable power via different events for both TBD and HMM-based decoders ($M = 4$, standard air in the medium, $\Phi \approx 1$). The HMM decoder can increase the monitoring distance by three orders of magnitude.

ply from a battery. In this section, we examine chemical process monitoring assuming self-powered sensor nodes capable of harvesting energy from the embedded environment. This section has two goals. First, we want to demonstrate the conceptual feasibility of using thermoelectric energy harvesting signatures to monitor chemical reactions using a pyroelectric-based SEMON (Pyro-SEMON). Second, we want to show that by exploiting the fact that chemical reactions can be modeled as a Markov chain, the HMM decoder can be used to improve the detection accuracy. We begin with a review on the energy harvesting mechanism.

6.1 Pyroelectric energy harvester

A pyroelectric nanogenerator converts any temperature variation to electricity where the pyroelectric current generated is proportional to the temperature change. The detectable current $i(t)$ of a pyroelectric material is proportional to the rate of change of its temperature and can be expressed as [49]:

$$i(t) = P_C \times A \times (\frac{dT(t)}{dt}) \tag{6.1}$$

where P_C is the pyroelectric current coefficient of the material, which is measured experimentally by measuring the output current [31]. A is the surface area of the electrode connected to the pyroelectric material during measurements. A larger electrode will collect larger number of electrons and hence the measured current will increase. The dT/dt denotes the temporal temperature

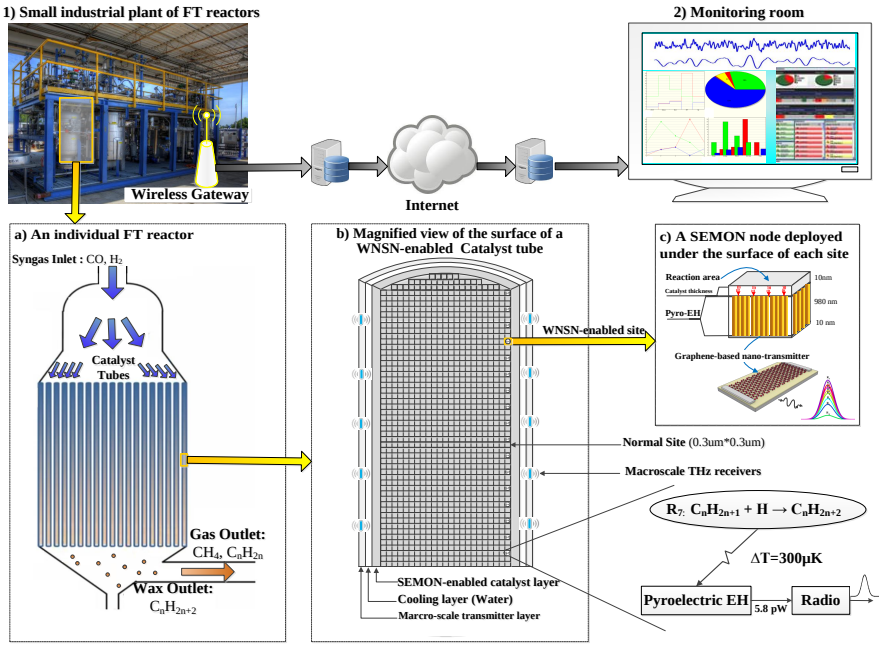

Figure 6.1: Overall microscopic monitoring of chemical reactor using SEMON nodes. (1) a picture from a small industrial Velocys pilot plant of FT reactors [45]. (2) data from the reactor will be collected and transferred to the monitor room for further analysis. (a) schematic of a single chemical reactor. (b) a snapshot cross section of a catalyst tube. (b) a schematic of the inner surface of the catalyst that its sites have been equipped with Pyro-SEMON node. (c) the working principle of the Pyro-SEMON nodes in reaction monitoring. As an example, an R7 reaction raises the site temperature by $300\mu K$, which generates a 5.8 pW of instantaneous power supply for the radio.

gradient. Larger changes in temperature over shorter periods generate larger output current. The pyroelectric current coefficient depends on the material of the nanogenerator. In this work we use the zinc oxide pyroelectric nanogenerator proposed in [49] which has a coefficient of $1.2-1.5$ nC/cm^2 K. The harvested power is then derived as:

$$P_H = I^2 \times R \tag{6.2}$$

where R is the device resistance, which has the value of 50 MΩ in [50].

6.2 Reaction monitoring using a Pyroelectric SEMON

Chemical reactions can be exothermic, i.e., they produce heat, or endothermic, i.e., they consume heat from the environment. This *thermal effect* of chemical reactions could be used as a practical source of energy for powering a Pyro-SEMON node.

Figure 6.1 illustrates the overall process of energy harvesting and communication of a Pyro-SEMON nanomotes used to monitor a given chemical reactor

at the molecular level. Figure 6.1a depicts a chemical reactor which contains many tubes designed to maximise the contact surface area between chemical reactants and the catalyst which lined the inner surface of the tubes. The catalyst surface (see Figure 6.1b) has many sites and chemical reactions will take place at these sites. Our proposal is to deploy a Pyro-SEMON node at a catalyst site to monitor the reactions that are taking place at that site. We assume that remote stations can be deployed on the outer surface of the tubes as shown in Figure 6.1b. The space between the inner and outer surfaces of the tubes is a space where cooling water flows. This implies that the communication medium between the Pyro-SEMON nodes and the remote stations is water.

Table 6.1: Surficial Reactions and Released Energy in KJ/mol for Fischer-Tropsch Synthesis

	Reaction	**Released Energy** (KJ/mole)
	Water Formation	
R_1	$O_{(s)} + H_{(s)} \longrightarrow OH_{(s)} + s$	103.80±0.96
R_2	$OH_{(s)} + H_{(s)} \longrightarrow H_2O_{(s)} + s$	86.22±0.62
	Chain Initiation	
R_3	$C_{(s)} + H_{(s)} \longrightarrow CH_{(s)} + s$	77.66 ±0.7
R_4	$CH_{(s)} + H_{(s)} \longrightarrow CH_{2(s)} + s$	11.94±0.1
R_5	$CH_{2(s)} + H_{(s)} \longrightarrow CH_{3(s)} + s$	61.88±0.5
	Chain Growth	
R_6	$C_nH_{2n+1(s)} + CH_{2(s)} \longrightarrow C_mH_{2m+1(s)}$ (m=n+1)	44.79±0.43
	Hydrogenation to Paraffin (HTP)	
R_7	$C_nH_{2n+1(s)} + H_{(s)} \longrightarrow C_nH_{2n+2} + 2\,s$	117.75±0.67
	β -Dehydrogenation to Olefin (DTO)	
R_8	$C_nH_{2n+1(s)} \longrightarrow C_nH_{2n} + H_{(s)}$	96.27±0.5

The production (or consumption) of heat by the reactions would increase (or decrease) the temperature of the site. This instantaneous temperature variation can be converted to electrical energy by the pyroelectric energy harvester on a Pyro-SEMON node. The harvested power can be directly used to generate and transmit a radio pulse to a nearby remote station. If each chemical reaction produces or consumes a different amount of heat, then this amount of heat can be used as a signature of the chemical reaction. Therefore, we can apply the SEMON architecture and use the energy of the received pulse to detect the chemical reactions taking place at a Pyro-SEMON node[1]. In this paper, we consider the communication between a SEMON node and a remote station. If a remote station is to receive from multiple SEMON nodes, then some multiplex-

[1]Note that in this paper we assume that the remote station uses an energy detector to detect the pulses. This means that we will not be able to distinguish between an exothermic reaction and an endothermic reaction that generate the same amount of heat. These two reactions will create temperature gradients of the same magnitude but in different directions. This means the pyroelectric currents generated by these two reactions flow in the opposite directions, which in turn means the pulses sent by the Pyro-SEMON node will have the same amplitude but opposite phases. It is not possible to use an energy detector alone to distinguish these pulses because an energy detector is blind to the phase. However, if we choose a more complex detector that can detect the phase, then these reactions become distinguishable.

ing scheme is required. One possibility is for the SEMON nodes to use different pulse shapes so that the frequency contents of the pulses are different. In this case, the remote station can use a filter bank to demultiplex and passed the demultiplexed signal through an energy detector. We will not study multiplexing and demultiplexing in this paper, and will leave it as future work.

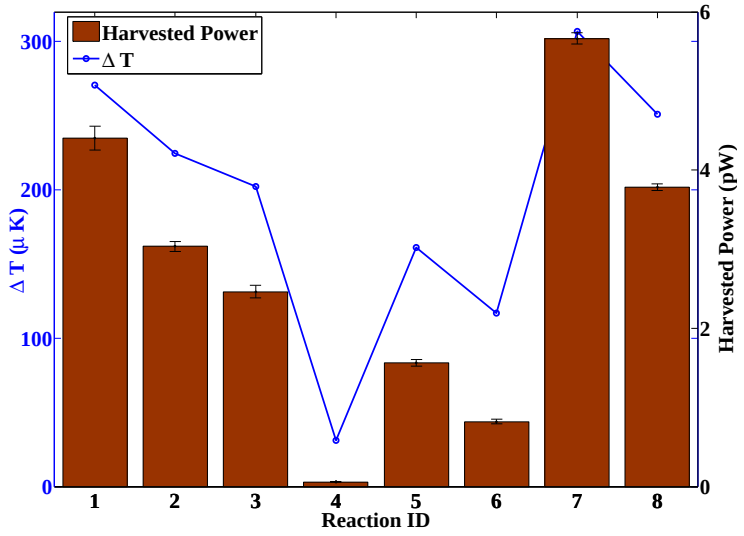

Figure 6.2: Estimating harvested power from temperature rise in a site using the pyroelectric model of [49]. A site is assumed to have a mass of 1.5 fg and thermal capacity of 0.45 J/gK. Each reaction involves two molecules and is assumed to last for a pico second. The average harvested power via 8 reactions is 2.7 pW.

In order to make our discussion concrete, we have selected the Fischer-Tropsch Synthesis (FTS) [2] as a case study. However, the discussion and methodology in this paper is entirely general. FTS synthesis is a major process for converting natural gas to liquid hydrocarbons in a chemical reactor. FTS involves a complex set of chemical reactions of many chemical species. However, it is possible to classify all the chemical reactions into eight categories of chemical reactions [33]. We denote these eight categories as R_1 to R_8 and they are listed in Table 6.1. FTS is a highly exothermic process, generating heat at an extremely high rate. Commercial FTS reactors employ significant cooling infrastructure, such as continuously circulation of water along the outer surface of the reactor, to control the temperature within the reactor. High rate of heat generation means that the pyroelectric energy harvesting model discussed earlier would be able to generate significant amount of power whenever a reaction takes place at a site.

We now estimate the amount of harvestable power by using pyroelectric nanogenerators. We begin with the energy released by each category of reactions, which is given in the last column of Table 6.1 [33]. We first need to derive the rate of temperature change, which can be obtained as $\frac{dT}{dt} \approx \frac{\Delta T}{t_{\text{reaction}}}$, where ΔT is the amount of temperature rise in the site due to the reaction heat and

t_{reaction} is the reaction time. The temperature rise ΔT can be obtained directly from the heat formula as $\Delta T = \frac{H}{C_p \times m}$, where H is the amount of heat released by the chemical reaction (Table 6.1) to the site, C_p is the specific heat capacity of the catalyst ($0.45\ J/gK$ for iron), and m is the mass of the catalyst site (which is 1.5fg assuming each site has a surface area of $0.3\mu m \times 0.3\mu m$). By assuming a reaction time $t_{\text{reaction}} = 1$ps, we have $\frac{dT}{dt} \approx \Delta T \times 10^{12}$. This means that even for a small ΔT, we can expect a significant rate of change in the temperature and eventually the harvested power. Reaction recognition is possible from the pulse energy at the remote station if different types of reactions produce different amounts of heat, i.e., if they have very different energy signatures. Figure 6.2 shows the temperature rise in each site of an iron-based catalyst and the resulting harvested power $P_{h,i}$ for i-th category of reactions, using the pyroelectric model of [49]. We can see that there are significant differences in the amount of energy generation by each category of reactions, giving hope that the proposed energy-signature-based event monitoring method would work for FTS. However, as explained earlier, the actual reaction recognition accuracy would depend on the amount of noise and signal attenuation experienced by the transmitted pulses and also the type of the decoder in the remote station.

6.3 Threshold based decoder

Given the harvestable power $P_{h,i}$ $(i = 1, ..., 8)$ for each category of reactions, we can use the receiver model in Section 4.2 to determine the Gaussian distribution of the energy received by the remote station. After that, we can use the procedure in Section 4.3 to determine the thresholds required for TBD decoding.

6.4 HMM-based decoder

The HMM decoder assumes that events generated can be modeled by a Markov chain. For this particular application, the events are the categories of chemical reactions in the FTS, which are labeled as $R_1, ..., R_8$. The state space of the Markov chain is therefore $\{R_1, ..., R_8\}$. We will need to derive the parameters of the Markov chain, which are the initial probability of the states and the transition probabilities. We have chosen to determine these parameters empirically. We begin with the fact that chemical reactions can be modeled by a CTMC whose state vector is the number of molecules of each chemical species and state transitions are caused by chemical reactions [16]. We then use the Stochastic Simulation Algorithm (SSA) [15], which is a method to simulate chemical reactions or CTMC, to simulate the FTS. In particular, we record the sequence of chemical reactions taking place in the simulation. By mapping the chemical reactions to the category that they belong, we obtain a sequence of $R_1, ..., R_8$. By repeating the simulation a number of times, we determine the initial state probability and the transition probability matrix. The transition matrix for FTS was found to be:

$$T_{FTS}^{\Phi=1.3} = \begin{pmatrix} 0.051 & 0.300 & 0.220 & 0.154 & 0.080 & 0.024 & 0.044 & 0.112 \\ 0.004 & 0.045 & 0.433 & 0.211 & 0.083 & 0.028 & 0.044 & 0.152 \\ 0.005 & 0.041 & 0.250 & 0.440 & 0.079 & 0.019 & 0.055 & 0.109 \\ 0.005 & 0.033 & 0.203 & 0.226 & 0.328 & 0.090 & 0.040 & 0.075 \\ 0.003 & 0.017 & 0.173 & 0.095 & 0.079 & 0.171 & 0.145 & 0.317 \\ 0.002 & 0.008 & 0.065 & 0.038 & 0.029 & 0.179 & 0.079 & 0.599 \\ 0.008 & 0.033 & 0.427 & 0.209 & 0.070 & 0.022 & 0.052 & 0.180 \\ 0.016 & 0.068 & 0.288 & 0.234 & 0.224 & 0.046 & 0.067 & 0.057 \end{pmatrix},$$

This Markov chain is found to have an entropy of 1.3. Given that the maximum possible entropy for a Markov chain with 8 states is 3, the entropy of the Markov chain for FTS is relatively low.

6.5 Methodology

In order to simulate the observations for TBD and HMM decoding. We start by simulating the FTS using the SSA algorithm. We assume that FTS is supplied with an initial feeding gas with 100 CO molecules and 250 H atoms. We use a conventional FTS reactor with the following reaction rate constants for the 8 reactions categories: 0.2 for R_1, 2 for R_2 and 7 for R_3 to R_8. The output of SSA is a sequence of chemical reactions that have taken place.

We assume an ideal pyroelectric nanogenerator that converts all the heat released by the chemical reactions into electrical energy. For each chemical reaction, we assume the Pyro-SEMON node generates a Gaussian pulse with a width of 100 fs. Since the transmission medium consists of water, we use the molecular absorption coefficient of liquid water in the receiver model to determine the probability distributions of the detected energy at the remote station. These probability distributions allow us to generate the sequence of observations to be supplied to the TBD and HMM decoders.

We would like to point out that water is a challenging transmission medium to work with for terahertz band signals. This is because water has a higher molecule absorption coefficient compared with many other chemical species. HITRAN database [4] only contains absorption coefficient,$K(f)$, of the gaseous molecules but in our case study the communication medium is composed of pure liquid water which is not available in HITRAN. There are a lots of studies in the literature attempting to measure the absorption coefficient of liquid water in different spectrum which can be found in [1] but only few of them have studied the terahertz band. In this study, we use the molecular absorption of the liquid water extracted from [34].

6.6 Results

We vary the distance d between the Pyro-SEMON node and the remote station from $10\mu m$ to 1m. For each distance, we simulate the FTS 50 times. We use both TBD and HMM as decoders, and determine the average decoding error over 50 simulations. Figure 6.3 plots the average error against the distance d. The figure shows that the HMM decoder outperforms the TBD decoder. If we use the monitoring distance (which is defined as the distance with 10% decoding error) as the performance criterion, then the monitoring distance for TBD and HMM are, respectively, 0.15mm and 15cm. The monitoring distance offered by TBD, at 0.15mm, may not be appropriate for our chemical reactor architecture as the distance between the SEMON node and the remote station is limited. Furthermore, our results are obtained under the assumption that all the heat release is converted into energy in the pulse. Therefore, under non-ideal assumptions, the actual monitoring distance is expected to be even smaller. On the other hand, the HMM decoder offers a monitoring distance of 15cm, which is 3 orders of magnitude higher than that provide by TBD.

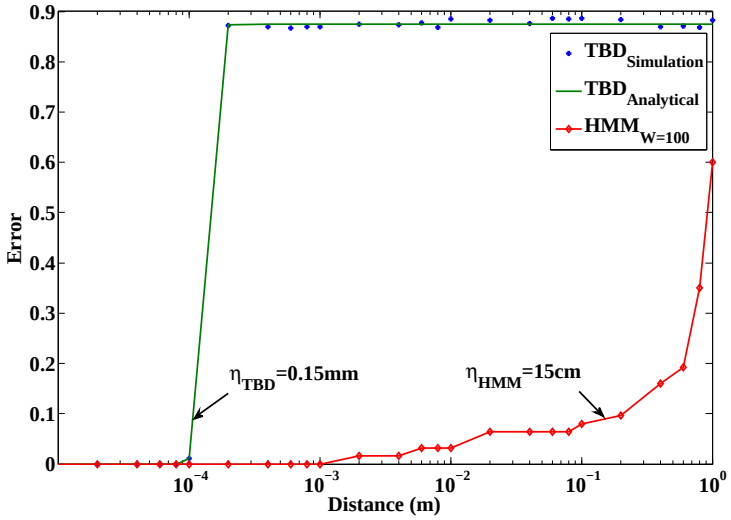

Figure 6.3: The average reaction recognition error via TBD over 30 distances ranging from $10\mu m$ to $1m$ that has been obtained from 50 iterations of SSA simulation.

7 Conclusions

We have proposed a simplified architecture for self-powered nanomotes composed of a nanoscale energy harvester and a nanoradio. It uses the energy signatures of monitored events to efficiently detect events at the remote station. By directly using the instantaneous harvested energy to transmit a pulse of proportional amplitude, the proposed architecture obviates the need for several conventional sensor node elements including the microprocessor, memory, and sensor. The architectural simplicity significantly reduces the total size and energy demand of the sensor node, which is important for WNSN.

We have proposed a simple threshold based decoder at the sink which is able to detect the events merely based on their received signal energies. Due to signal attenuation, which reduces the received energy difference between two different event pulses, accuracy diminishes as a function of distance. We have shown that event recognition accuracy can be significantly improved over larger distances by using the underlying probabilistic model between events as a hidden Markov model to improve the inference process at the sink.

The application of the proposed architecture has been explored with a real example of reaction monitoring within a chemical reactor. The numerical results confirmed the viability of accurate reaction recognition when a sensor node communicates with the sink in a single hop wireless transmission over a short distance.

Bibliography

[1] Optical Absorption of Water Compendium.

[2] A. Adesina. Hydrocarbon synthesis via Fischer-Tropsch reaction: travails and triumphs. *Applied Catalysis A: General*, 138(2):345–367, 1996.

[3] I. F. Akyildiz and J. M. Jornet. Electromagnetic wireless nanosensor networks. *Nano Communication Networks*, 1(1):3–19, 2010.

[4] Y. L. Babikov, I. E. Gordon, and S. N. Mikhailenko. Hitran on the web, a new tool for hitran spectroscopic data manipulation. In *the Proceeding of the ASA-HITRAN Conference*, Reims, France, Aug 29-31, 2012.

[5] P. Basu, P. Bhattacharyya, N. Saha, H. Saha, and S. Basu. The superior performance of the electrochemically grown ZnO thin films as methane sensor. *Sensors and Actuators B: Chemical*, 133(2):357–363, Aug. 2008.

[6] B. Bhatia, A. R. Damodaran, H. Cho, L. W. Martin, and W. P. King. High-frequency thermal-electrical cycles for pyroelectric energy conversion. *Journal of Applied Physics*, 116(19):194509, Nov. 2014.

[7] G. Cha, Y. Jia, and Y. Ju. High-power density pyroelectric energy harvesters incorporating switchable liquid-based thermal interfaces. In *Micro Electro Mechanical Systems (MEMS), 2012 IEEE 25th International Conference on*, pages 1241–1244, Jan 2012.

[8] G. Cheng, Z. Lin, L. Lin, Z.-l. Du, and Z. Wang. Pulsed Nanogenerator with Huge Instantaneous Output Power Density. *ACS nano*, 7(8):7383–7391, 2013.

[9] S. Cui and F. Xiong. M-ary energy detection of a Gaussian FSK UWB system. *EURASIP Journal on Wireless Communications and Networking*, 2014(1):87, 2014.

[10] L. L. Fields, J. P. Zheng, Y. Cheng, and P. Xiong. Room-temperature low-power hydrogen sensor based on a single tin dioxide nanobelt. *Applied Physics Letters*, 88(26):263102, 2006.

[11] Figaro Sensor. TGS 821: Special Sensor for Hydrogen Gas, 2012.

[12] J. Forney, G.D. The viterbi algorithm. *Proceedings of the IEEE*, 61(3):268–278, March 1973.

[13] L. A. Franco-Gasca, G. Herrera-Ruiz, R. Peniche-Vera, R. D. J. Romero-Troncoso, and W. Leal-Tafolla. Sensorless tool failure monitoring system for drilling machines. *International Journal of Machine Tools and Manufacture*, 46(3-4):381–386, Mar. 2006.

[14] K. Gaikwad and V. Narawade. HMM Classifier for Human Activity Recognition. *An International Journal on Computer Science & Engineering (CSEIJ)*, 2(4):27–36, 2012.

[15] D. Gillespie. Exact stochastic simulation of coupled chemical reactions. *The journal of physical chemistry*, 81(25):2340–2361, 1977.

[16] D. Gillespie. A rigorous derivation of the chemical master equation. *Physica A: Statistical Mechanics and its Applications*, 188:404–425, Sept. 1992.

[17] A. Goldsmith. *Wireless Communications*. Cambridge University Press, Cambridge, 2005.

[18] M. Han, X. Zhang, B. Meng, W. Liu, and W. Tang. r-Shaped hybrid nanogenerator with enhanced piezoelectricity. *ACS nano*, 7(10):8554–8560, 2013.

[19] M. Han, X.-S. Zhang, X. Sun, B. Meng, W. Liu, and H. Zhang. Magnetic-assisted triboelectric nanogenerators as self-powered visualized omnidirectional tilt sensing system. *Scientific reports*, 4:4811, Jan. 2014.

[20] T. Helbling, S. Drittenbass, L. Durrer, C. Roman, and C. Hierold. Ultra small single walled carbon nanotube pressure sensors. In *Micro Electro Mechanical Systems, 2009. MEMS 2009. IEEE 22nd International Conference on*, pages 575–578, Jan 2009.

[21] J. Jornet and I. Akyildiz. Channel modeling and capacity analysis for electromagnetic wireless nanonetworks in the terahertz band. *IEEE Transactions on Wireless Communications*, 10(10):3211–3221, 2011.

[22] S. Khalifa, M. Hassan, and A. Seneviratne. Pervasive self-powered human activity recognition without the accelerometer. In *Pervasive Computing and Communications (PerCom), 2015 IEEE International Conference on*, pages 79–86, March 2015.

[23] S. Khalifa, M. Hassan, A. Seneviratne, and S. Das. Energy-harvesting wearables for activity-aware services. *Internet Computing, IEEE*, 19(5):8–16, Sept 2015.

[24] K. Kim, I. Akbar, K. Bae, J.-S. Um, C. Spooner, and J. Reed. Cyclostationary approaches to signal detection and classification in cognitive radio. In *New Frontiers in Dynamic Spectrum Access Networks, 2007. DySPAN 2007. 2nd IEEE International Symposium on*, pages 212–215, April 2007.

[25] S. N. Kumar and K. Gayithri. Real time glucose monitoring system based on enzymatic nanosensor. In *International Conference on Advanced Nanomaterials & Emerging Engineering*, pages 379–382, India, 2013.

[26] P.-H. Kuo, S.-S. Lu, J.-C. Kuo, Y.-J. Yang, T. Wang, Y.-L. Ho, and M.-F. Chen. A hydrogel-based implantable wireless cmos glucose sensor soc. In *Circuits and Systems (ISCAS), 2012 IEEE International Symposium on*, pages 994–997, May 2012.

[27] Y. Lee and S. Cho. Activity recognition using hierarchical hidden markov models on a smartphone with 3D accelerometer. *Hybrid Artificial Intelligent Systems*, pages 460–467, 2011.

[28] W. Li, D. Li, and J. Ni. Diagnosis of tapping process using spindle motor current. *International Journal of Machine Tools & Manufacture*, 43:73–79, 2003.

[29] Y. Liao, H. Yao, and A. Lingley. A 3-cmos glucose sensor for wireless contact-lens tear glucose monitoring. *IEEE Journal of Solid-State Circuits*, 47(1):335–344, 2012.

[30] C.-C. Lin and J.-G. Hwu. Performance enhancement of metal-oxide-semiconductor tunneling temperature sensors with nanoscale oxides by employing ultrathin Al2O3 high-k dielectrics. *Nanoscale*, 5(17):8090–7, Sept. 2013.

[31] D. Lingam, A. R. Parikh, J. Huang, A. Jain, and M. Minary-Jolandan. Nano/microscale pyroelectric energy harvesting: challenges and opportunities. *International Journal of Smart and Nano Materials*, 4(4):229–245, Dec. 2013.

[32] L. Liu, T. Zhang, Q. Qi, L. Zhang, W. Chen, and B. Xu. A novel micro-structure ethanol gas sensor with low power consumption based on La0.7Sr0.3FeO3. *Solid-State Electronics*, 51(7):1029–1033, July 2007.

[33] G. Lozano-Blanco and J. Thybaut. Single-Event Microkinetic Model for Fischer Tropsch Synthesis on Iron-Based Catalysts. *Industrial & Engineering Chemistry Research*, 47:5879–5891, 2008.

[34] G. M. Hale and R. Marvin. Optical Constants of Water in the 200-nm to 200-um Wavelength Region. *APPLIED OPTICS*, 12(3):555–563, Dec. 1973, data available at: http://omlc.org/spectra/water/data/hale73.dat.

[35] W. Mickelson, A. Sussman, and A. Zettl. Low-power, fast, selective nanoparticle-based hydrogen sulfide gas sensor. *Applied Physics Letters*, 2:2–6, 2012.

[36] K. Murphy. Hidden Markov Model (HMM) Matlab Toolbox, 2004.

[37] K.-I. Park, S. Xu, Y. Liu, G.-T. Hwang, S.-J. L. Kang, Z. L. Wang, and K. J. Lee. Piezoelectric BaTiO thin film nanogenerator on plastic substrates. *Nano letters*, 10(12):4939–43, Dec. 2010.

[38] A. Ponzoni, E. Comini, G. Sberveglieri, J. Zhou, S. Z. Deng, N. S. Xu, Y. Ding, and Z. L. Wang. Ultrasensitive and highly selective gas sensors using three-dimensional tungsten oxide nanowire networks. *Applied Physics Letters*, 88(20):203101, 2006.

[39] P. Sadeghi, R. A. Kennedy, P. B. Rapajic, and R. Shams. Finite-State Markov Modeling of Fading Channels. *IEEE SIGNAL PROCESSING MAGAZINE*, 1(September 2008):57–80, Sept. 2008.

[40] R. Singh and S. Mishra. Temperature monitoring in wireless sensor network using zigbee transceiver module. In *Power, Control and Embedded Systems (ICPCES), 2010 International Conference on*, pages 1–4, Nov 2010.

[41] R. Singh, S. Mishra, and P. Joshi. Pressure monitoring in wireless sensor network using zigbee transceiver module. In *Computer and Communication Technology (ICCCT), 2011 2nd International Conference on*, pages 225–229, Sept 2011.

[42] M. Sonnaillon. Online sensorless induction motor temperature monitoring. *IEEE TRANSACTIONS ON ENERGY CONVERSION*, 25(2):273–280, 2010.

[43] E. technologies. MiCS-2710 NO2 Sensor, 2008.

[44] L. C. Tien, H. T. Wang, B. S. Kang, F. Ren, P. W. Sadik, D. P. Norton, S. J. Pearton, and J. Lin. Room-Temperature Hydrogen-Selective Sensing Using Single Pt-Coated ZnO Nanowires at Microwatt Power Levels. *Electrochemical and Solid-State Letters*, 8(9):G230, 2005.

[45] Velocys, http://www.velocys.com.

[46] Z. L. Wang and J. Song. Piezoelectric nanogenerators based on zinc oxide nanowire arrays. *Science (New York, N.Y.)*, 312(5771):242–6, Apr. 2006.

[47] H. Wei, J. He, and J. Tan. Layered hidden Markov models for real-time daily activity monitoring using body sensor networks. *Knowledge and Information Systems*, 29(2):479–494, June 2011.

[48] S. Xu, B. J. Hansen, and Z. L. Wang. Piezoelectric-nanowire-enabled power source for driving wireless microelectronics. *Nature communications*, 1(7):93, Jan. 2010.

[49] Y. Yang, W. Guo, K. C. Pradel, G. Zhu, Y. Zhou, Y. Zhang, Y. Hu, L. Lin, and Z. L. Wang. Pyroelectric nanogenerators for harvesting thermoelectric energy. *Nano letters*, 12(6):2833–8, June 2012.

[50] Y. Yang, S. Wang, Y. Zhang, and Z. L. Wang. Pyroelectric nanogenerators for driving wireless sensors. *Nano letters*, 12(12):6408–13, Dec. 2012.

[51] Y. Yang, Y. Zhou, J. Wu, and Z. Wang. Single micro/nanowire pyroelectric nanogenerators as self-powered temperature sensors. *ACS nano*, 6(9):8456–8461, 2012.

[52] E. Zarepour, A. A. Adesina, M. Hassan, and C. T. Chou. Innovative approach to improving gas-to-liquid fuel catalysis via nanosensor network modulation. *Industrial and Engineering Chemistry Research*, 53(14):5728–5736, 2014.

[53] E. Zarepour, M. Hassan, C. T. Chou, and A. A. Adesina. Remote Detection of Chemical Reactions using Nanoscale Terahertz Communication Powered by Pyroelectric Energy Harvesting. In *the proceedings of the 2th ACM International Conference on Nanoscale Computing and Communication*, Boston, Massachusetts, USA, September 21-22, 2015.

[54] H. Zhang, Y. Yang, Y. Su, J. Chen, C. Hu, Z. Wu, Y. Liu, C. Ping Wong, Y. Bando, and Z. L. Wang. Triboelectric nanogenerator as self-powered active sensors for detecting liquid/gaseous water/ethanol. *Nano Energy*, 2(5):693–701, Sept. 2013.

[55] M. Zhang, C. Fung, G. Chow, W. Li, and P. Leong. Parylene-c embedded cnt-based mems piezoresistive pressure sensors using dep nanoassembly. In *Nanotechnology, 2006. IEEE-NANO 2006. Sixth IEEE Conference on*, volume 2, pages 802–805, June 2006.

[56] P. Zhang, B. Lu, and T. Habetler. A remote and sensorless stator winding resistance estimation method for thermal protection of soft-starter-connected induction machines. *IEEE Transactions on INDUSTRIAL ELECTRONICS*, 55(10):3611–3618, 2008.

[57] Y. Zhou, D. J. Apo, and S. Priya. Dual-phase self-biased magnetoelectric energy harvester. *Applied Physics Letters*, 103(19):192909, 2013.

[58] G. Zhu, R. Yang, S. Wang, and Z. L. Wang. Flexible high-output nanogenerator based on lateral ZnO nanowire array. *Nano letters*, 10(8):3151–5, Aug. 2010.